ANALYSIS OF ^{6}Li(^{3}He,d)^{7}Be TRANSFER REACTION FOR DIFFERENT APPROACHES

M. Aygun[a], Z. Aygun[b], N. Karaali[a]

[a]Department of Physics, Bitlis Eren University, Bitlis, 13000, Turkey
[b]Vocational School of Technical Sciences, Bitlis Eren University
Bitlis, 13000, Turkey

Received 23 February 2023, accepted 30 May 2023, published online 6 June 2023

In this study, the ^{6}Li(^{3}He,d)^{7}Be transfer reaction at 33.3 and 34 MeV is analyzed in the framework of the optical model by using the FRESCO code based on the distorted wave Born approximation (DWBA) method for temperature-dependent and temperature-independent density distributions, different nuclear potentials, and different nucleon–nucleon interactions. The nuclear potential is assumed to have real and imaginary parts in the entrance and exit channels together with the Coulomb potential. The similarities and differences of all the different approaches are discussed, and alternative density, alternative nuclear potential, and alternative nucleon–nucleon interactions are suggested.

DOI:10.5506/APhysPolB.54.5-A1

1. Introduction

One of the most important goals of nuclear physics is to understand the origin of the matter in the Universe. In this context, nuclear reactions are one of the important tools, and the transfer reaction is one of them. A transfer reaction is a direct reaction transferring one or more nucleons between the projectile and the target. It is well known that transfer reactions based on the light-ion projectiles provided an important contribution obtaining information about nuclear physics and nuclear structure [1]. Transfer reactions are assumed as a common instrument to obtain useful information about astrophysical processes. They are also crucial for experimental nuclear astrophysics due to providing an opportunity to study nuclei formed in stellar reactions that are hard or impossible to generate in the laboratory [2].

Solving the transfer reaction is a computationally intensive process. It can be studied with different theoretical approaches such as the distorted wave Born approximation (DWBA), adiabatic distorted wave approximation (ADWA), coupled reaction channel (CRC), or coupled channel Born

approximation (CCBA). The DWBA is one of the most preferred theoretical models within the framework of the optical model (OM) which is one of successful ways in describing the transfer reaction. Determining of optical model parameters is necessary for the theoretical analysis of reactions under examination. For example, the transfer cross sections based on DWBA analysis are very sensitive to changing of the optical potential parameters. In this context, a lot of attempts for the extraction of optical potential parameters of transfer reactions were performed. However, the investigation of potential parameters of transfer reactions is still an important issue. One of the aims of the present work is to determine the potential parameters for different nuclear cases.

In previous years, the angular distribution of the ^{6}Li(^{3}He,d)^{7}Be transfer reaction was measured at different energies, and was analyzed by using the DWBA method [3, 4]. Recently, new experimental data of the ^{6}Li(^{3}He,d)^{7}Be transfer reaction at 34 MeV was measured by Burtebayev *et al.* [5]. They analyzed the data over CRC and DWBA calculations. However, this reaction has not been evaluated within the scope of different approaches such as density distribution, temperature, nuclear potential, and nucleon–nucleon (NN) interactions. We believe that the study to be done for this purpose will be important in the analysis of both this reaction and other transfer reactions.

In the present work, we reanalyze the ^{6}Li(^{3}He,d)^{7}Be transfer reaction at 34 MeV for the temperature-dependent and temperature-independent density distributions, different nuclear potentials, and different NN interactions. To make a comparative analysis, the same procedures are performed for the 33.3 MeV energy value of the same reaction. The calculations are carried out by using the FRESCO code based on the DWBA method. The theoretical results are compared with each other as well as with the experimental data, and alternative density, alternative nuclear potential, and alternative nucleon–nucleon interactions are proposed.

Section 2 presents the calculation formalism for the ^{6}Li(^{3}He,d)^{7}Be transfer reaction. Sections 3 and 4 show the temperature-independent and temperature-dependent density distributions, respectively. Sections 5 and 6 display different nuclear potentials and different nucleon–nucleon interactions, respectively. Section 7 provides the results and discussion. Section 8 displays the summary and conclusions.

2. Calculation details

For the theoretical analysis of the ^{6}Li(^{3}He,d)^{7}Be reaction, the various interactions should be considered: entrance channel (^{3}He+^{6}Li), exit channel ($d + {}^{7}$Be), core–core ($d + {}^{6}$Li), and binding potentials ($p + d$ and $p + {}^{6}$Li). The ^{3}He projectile is assumed as the composite system $^{3}\text{He} = d + p$ (see

Fig. 1) in the entrance channel. Then, one p is transferred to the ^{6}Li target, and thus it leads to the composite target-like fragment $^{7}\mathrm{Be} = {}^{6}\mathrm{Li} + p$ in the exit channel. Generally, it can be said that the interaction potentials for the entrance and exit channels of transfer reactions are different [6]. Thus, knowledge of interaction potentials is needed for the partitions. The calculation procedure associated with these potentials is described below.

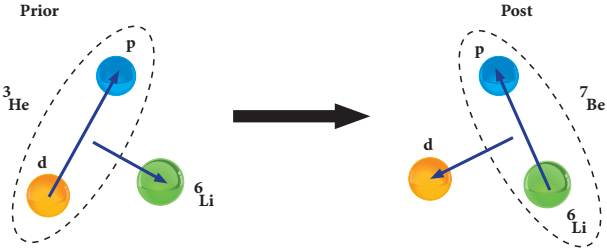

Fig. 1. The scheme of the ^{6}Li(^{3}He,d)^{7}Be transfer reaction.

2.1. Entrance channel ($^{3}He + {}^{6}Li$)

The potentials applied for the entrance channel, which are a dominant cause of theoretical uncertainty in the analysis of the transfer reactions, play a significant role. Therefore, we examine the effect of the entrance channel on the transfer cross section by using different approaches.

The nuclear potential of the entrance channel consists of the real and imaginary potentials. To obtain the real potential, both the optical model and the double-folding model are used via the FRESCO [7] and DFPOT [8] codes which are used extensively in the analysis of various nuclear reactions [9–14]. Thus, the real part is calculated for the temperature-dependent and temperature-independent density distributions, different nuclear potentials, and different NN interactions, and all of these interactions are summarized below. Additionally, the spin-orbit potential for the real part is assumed and written as

$$V_{\mathrm{so}}(r) = -\left(\frac{\hbar}{m_{\pi}c}\right)^{2}\left(\vec{L}\bullet\vec{S}\right)\frac{V_{\mathrm{so}}}{a_{\mathrm{so}}r}\frac{\exp\left(\frac{r-R_{\mathrm{so}}}{a_{\mathrm{so}}}\right)}{\left[1+\exp\left(\frac{r-R_{\mathrm{so}}}{a_{\mathrm{so}}}\right)\right]^{2}}, \tag{1}$$

where V_{so}, R_{so}, and a_{so} are the depth, radius, and diffuseness parameters of the spin-orbit potential, respectively.

The imaginary potential is in the Woods–Saxon volume form shown by

$$W(r) = -W_{0}\left[1+\exp\left(\frac{r-R_{w}}{a_{w}}\right)\right]^{-1}, \tag{2}$$

where W_0 is the depth, R_w is the radius, and a_w is the diffuseness parameter.

2.2. Exit channel ($d + {}^{7}Be$)

The nuclear potential of the exit channel is thought as the real, the imaginary, and the spin-orbit potentials. The real part of the optical potential is

$$V(r) = V_0 \left[1 + \exp\left(\frac{r - R_v}{a_v}\right)\right]^{-1}, \tag{3}$$

and the Woods–Saxon potential is in the surface absorption form shown by

$$W_d(r) = -4a_d W_d \frac{d}{dr}\left[1 + \exp\left(\frac{r - R_d}{a_d}\right)\right]^{-1}, \tag{4}$$

where V_0 and W_d are the depths, R_v and R_d are the radii, and a_v and a_d are diffuseness parameters. The spin-orbit potential is of the same form as in Eq. (1).

2.3. Core–core ($d + {}^{6}Li$)

The core–core potential, which means the interaction between core and core nuclei contains the real, imaginary, and spin-orbit potentials in the Woods–Saxon form. As a result, the nuclear potential is in the same form as the potential of the exit channel.

2.4. Binding potentials

Finally, the binding potentials for the ^{6}Li(^{3}He,d)^{7}Be transfer reaction can be evaluated as

(1) binding potential: entrance potential,

(2) binding potential: exit channel.

The binding potential for the entrance potential is $p + d$, and the binding potential for the exit channel is $p + {}^{6}$Li. Only the real potential is assumed and taken in the same form as in Eq. (3) with the Woods–Saxon potential having standard geometry parameters $r_0 = 1.25$ fm and $a = 0.65$ fm. Its depth is determined from the binding energies.

3. Density distributions of ^{3}He nucleus

3.1. Gauss 1 (G1)

The G1 density is given as

$$\rho(r) = \rho_0 \exp\left(-\alpha r^2\right), \tag{5}$$

where ρ_0 and α values, respectively, are 0.2201 fm^{-3} and 0.5505 fm^{-2} [15].

3.2. Gauss 2 (G2)

The G2 density is in the following form:

$$\rho(r) = \rho_0 \exp\left(-\beta r^2\right) , \tag{6}$$

where ρ_0 and β values, respectively, are 0.20816 fm^{-3} and 0.53047 fm^{-2} [16].

3.3. Ngô–Ngô (Ngo)

The Ngo density can be formulated as [17, 18]

$$\rho_i(r) = \frac{\rho_{0i}}{1 + \exp\left(\frac{r-C}{0.55}\right)} , \qquad (i = n, p) , \tag{7}$$

where

$$\rho_{0n(0p)} = \frac{3}{4\pi}\frac{N(Z)}{A}\frac{1}{r^3_{0n(0p)}} , \qquad C = R\left(1 - \frac{1}{R^2}\right) , \qquad R = \frac{NR_n + ZR_p}{A} , \tag{8}$$

with

$$R_n = \left(1.1375 + 1.875 \times 10^{-4} A\right) A^{1/3} , \qquad R_p = 1.128 A^{1/3} . \tag{9}$$

In the calculations, $\rho_{0n(0p)}$ are 0.0539873(0.11089), and C are 1.01884, respectively.

3.4. Schechter (S)

The parameters of S density which have the $2pF$ shape are taken as [19]

$$\rho_0 = 0.0930316 \text{ fm}^{-3} , \qquad R_0 = 1.49994 \text{ fm} , \quad \text{and} \quad a = 0.54 \text{ fm}. \tag{10}$$

4. Temperature-dependent density

Here, we examine temperature-dependent case of the entrance channel of the ^{6}Li(^{3}He,d)^{7}Be transfer reaction. For this, we use the $2pF$ density for different temperatures as given below [20]

$$\rho_i(r) = \frac{\rho_{0i}(T)}{\left[1 + \exp\left(\frac{r - R_{0i}(T)}{a_i(T)}\right)\right]} , \tag{11}$$

where the central density, ρ_{0i}, is written as

$$\rho_{0i}(T) = \frac{3A_i}{4\pi R^3_{0i}(T)}\left[1 + \frac{\pi^2 a_i^2(T)}{R^2_{0i}(T)}\right]^{-1} , \tag{12}$$

the half-density radius, $R_{0i}(T=0)$, is given by

$$\begin{aligned} R_{0i}(T=0) &= 0.90106 + 0.10957A_i - 0.0013A_i^2 \\ &\quad +7.71458\times10^{-6}A_i^3 - 1.62164\times10^{-8}A_i^4\,, \end{aligned}$$

and the surface thickness parameter, $a_i(T=0)$, is parameterized as

$$\begin{aligned} a_i(T=0) &= 0.34175 + 0.01234A_i - 2.1864\times10^{-4}A_i^2 \\ &\quad +1.46388\times10^{-6}A_i^3 - 3.24263\times10^{-9}A_i^4\,. \end{aligned}$$

In order to calculate the real part of the nuclear potential at different temperatures, we apply temperature-dependent forms of $R_{0i}(T)$ and $a_i(T)$ parameters shown by [21]

$$R_{0i}(T) = R_{0i}(T=0)\left[1+0.0005T^2\right]\,, \tag{13}$$

$$a_i(T) = a_i(T=0)\left[1+0.01T^2\right]\,. \tag{14}$$

5. Proximity potentials

5.1. Proximity 1977 (Prox 77)

The Prox 77 potential [22, 23] is written as

$$V_N^{\text{Prox}\,77}(r) = 4\pi\gamma b\bar{R}\Phi\left(\zeta=\frac{r-C_1-C_2}{b}\right)\ \text{MeV}\,, \tag{15}$$

where

$$\bar{R}=\frac{C_1C_2}{C_1+C_2}\,,\qquad C_i=R_i\left[1-\left(\frac{b}{R_i}\right)^2+\ldots\right]\,. \tag{16}$$

The effective radius, R_i, is given by

$$R_i = 1.28A_i^{1/3} - 0.76 + 0.8A_i^{-1/3}\ \text{fm}\,,\qquad (i=1,2)\,. \tag{17}$$

The surface energy coefficient, γ, is assumed as

$$\gamma=\gamma_0\left[1-k_s\left(\frac{N-Z}{N+Z}\right)^2\right]\,, \tag{18}$$

where $N(Z)$, respectively, is the total number of neutrons (protons), $\gamma_0=0.9517$ MeV/fm^2, and $k_s=1.7826$ [24]. The universal function $\Phi(\zeta)$ is in the following form:

$$\Phi(\zeta)=\begin{cases} -\frac{1}{2}(\zeta-2.54)^2-0.0852(\zeta-2.54)^3\,, & \text{for } \zeta\le1.2511\,,\\ -3.437\,\exp\left(-\frac{\zeta}{0.75}\right)\,, & \text{for } \zeta\ge1.2511\,. \end{cases}$$

5.2. Proximity 1988 (Prox 88)

γ_0 and k_s values of the Prox 88 potential are taken as 1.2496 MeV/fm^2 and 2.3, respectively [25]. The other parameters are the same as Prox 77.

5.3. Broglia and Winther 1991 (BW 91)

The BW 91 potential [25] is taken as [26]

$$V_N^{\mathrm{BW\,91}}(r) = -\frac{V_0}{\left[1+\exp\left(\frac{r-R_0}{a}\right)\right]}\ \mathrm{MeV}\,, \tag{19}$$

where

$$V_0 = 16\pi\frac{R_1R_2}{R_1+R_2}\gamma a\,, \qquad a = 0.63\ \mathrm{fm}\,, \tag{20}$$

and

$$R_0 = R_1 + R_2 + 0.29\,, \quad R_i = 1.233A_i^{1/3} - 0.98A_i^{-1/3}\,, \qquad (i=1,2)\,, \tag{21}$$

with γ being

$$\gamma = \gamma_0\left[1 - k_s\left(\frac{N_\mathrm{p}-Z_\mathrm{p}}{A_\mathrm{p}}\right)\left(\frac{N_\mathrm{t}-Z_\mathrm{t}}{A_\mathrm{t}}\right)\right]. \tag{22}$$

γ_0 and k_s are 0.95 MeV/fm^2 and 1.8, respectively.

5.4. Akyüz–Winther (AW 95)

The only difference between the AW 95 and BW 91 potentials [26, 27] is

$$a = \left[\frac{1}{1.17\left(1+0.53\left(A_1^{-1/3}+A_2^{-1/3}\right)\right)}\right]\ \mathrm{fm}\,, \tag{23}$$

and

$$R_0 = R_1 + R_2\,, \qquad R_i = 1.2A_i^{1/3} - 0.09\,, \qquad (i=1,2)\,. \tag{24}$$

5.5. Bass 1973 (Bass 73)

Bass 73 as proximity potential [28, 29] is parameterized by [23]

$$V_N^{\mathrm{Bass\,73}}(r) = -\frac{da_sA_1^{1/3}A_2^{1/3}}{R_{12}}\exp\left(-\frac{r-R_{12}}{d}\right)\ \mathrm{MeV}\,, \tag{25}$$

where

$$R_{12} = 1.07\left(A_1^{1/3}+A_2^{1/3}\right)\,, \qquad d = 1.35\ \mathrm{fm}\,, \qquad \text{and} \qquad a_s = 17\ \mathrm{MeV}\,. \tag{26}$$

5.6. Bass 1977 (Bass 77)

The Bass 77 potential [30] is assumed as [26]

$$V_N^{\text{Bass }77}(s) = -\frac{R_1 R_2}{R_1 + R_2}\phi\left(s = r - R_1 - R_2\right) \text{ MeV}\,, \tag{27}$$

where

$$R_i = 1.16A_i^{1/3} - 1.39A_i^{-1/3}\,, \qquad (i = 1, 2)\,, \tag{28}$$

$$\phi(s) = \left[A \exp\left(\frac{s}{d_1}\right) + B \exp\left(\frac{s}{d_2}\right)\right]^{-1}\,, \tag{29}$$

with $A = 0.030$ MeV^{-1}fm, $B = 0.0061$ MeV^{-1}fm, $d_1 = 3.30$ fm, and $d_2 = 0.65$ fm.

5.7. Bass 1980 (Bass 80)

The only difference between the Bass 80 and Bass 77 potentials is the function $\phi(s = r - R_1 - R_2)$, which is given by [25, 26]

$$\phi(s) = \left[0.033 \exp\left(\frac{s}{3.5}\right) + 0.007 \exp\left(\frac{s}{0.65}\right)\right]^{-1}\,, \tag{30}$$

and

$$R_i = R_s\left(1 - \frac{0.98}{R_s^2}\right)\,, \qquad R_s = 1.28A_i^{1/3} - 0.76 + 0.8A_i^{-1/3} \text{ fm}\,, \quad (i = 1, 2)\,. \tag{31}$$

5.8. Christensen and Winther 1976 (CW 76)

The CW 76 potential [31] is presented by [23] as

$$V_N^{\text{CW }76}(r) = -50\frac{R_1 R_2}{R_1 + R_2}\phi\left(s = r - R_1 - R_2\right) \text{ MeV}\,, \tag{32}$$

where

$$R_i = 1.233A_i^{1/3} - 0.978A_i^{-1/3} \text{ fm}\,, \qquad (i = 1, 2)\,, \tag{33}$$

$$\phi(s) = \exp\left(-\frac{r - R_1 - R_2}{0.63}\right)\,. \tag{34}$$

5.9. Ngô 1980 (Ngo 80)

The Ngo 80 potential which is the last proximity potential examined with this study is parameterized by [17]

$$V_N^{\mathrm{Ngo\,88}}(r) = \bar{R}\phi\,(r-\xi_1-\xi_2)\ \mathrm{MeV}\,, \tag{35}$$

$$\bar{R} = \frac{\xi_1\xi_2}{\xi_1+\xi_2}\,, \qquad \xi_i = R_i\left[1-\left(\frac{b}{R_i}\right)^2+\ldots\right]\,, \tag{36}$$

$$R_i = \frac{NR_{ni}+ZR_{pi}}{A_i}\,, \qquad (i=1,2)\,, \tag{37}$$

$$R_{pi} = r_{0pi}A_i^{1/3}\,, \qquad R_{ni} = r_{0ni}A_i^{1/3}\,, \tag{38}$$

$$r_{0pi} = 1.128\ \mathrm{fm}\,, \qquad r_{0ni} = 1.1375+1.875\times10^{-4}A_i\ \mathrm{fm}\,. \tag{39}$$

The universal function $\phi(\varsigma = r-\xi_1-\xi_2)$ (in MeV/fm) is written as

$$\Phi(\varsigma) = \begin{cases} -33+5.4\,(\varsigma-\varsigma_0)^2 & \text{for} \quad \varsigma<\varsigma_0\,, \\ -33\exp\left[-\frac{1}{5}\,(\varsigma-\varsigma_0)^2\right] & \text{for} \quad \varsigma\geq\varsigma_0\,, \\ \varsigma_0 = -1.6\ \mathrm{fm}\,. \end{cases}$$

6. Microscopic NN interaction

The effective NN interaction can be formulated as the sum of scalar and vector parts of the single-meson fields given by [32–34]

$$\nu_{NN}(r) = \frac{g_w^2}{4\pi}\frac{\mathrm{e}^{-m_w r}}{r}+\frac{g_\rho^2}{4\pi}\frac{\mathrm{e}^{-m_\rho r}}{r}-\frac{g_\sigma^2}{4\pi}\frac{\mathrm{e}^{-m_\sigma r}}{r}+\frac{g_2^2}{4\pi}r\,\mathrm{e}^{-2m_\sigma r}+\frac{g_3^2}{4\pi}r\frac{\mathrm{e}^{-3m_\sigma r}}{r}\,, \tag{40}$$

where g_w, g_ρ, and g_σ are the coupling constants, and m_w, m_ρ, and m_σ are the masses for w, ρ, and σ mesons, respectively. If the single-nucleon-exchange effect is added, equation (40) becomes

$$\begin{aligned}\nu_{NN}(r) = {} & \frac{g_w^2}{4\pi}\frac{\mathrm{e}^{-m_w r}}{r}+\frac{g_\rho^2}{4\pi}\frac{\mathrm{e}^{-m_\rho r}}{r}-\frac{g_\sigma^2}{4\pi}\frac{\mathrm{e}^{-m_\sigma r}}{r}+\frac{g_2^2}{4\pi}r\,\mathrm{e}^{-2m_\sigma r} \\ & +\frac{g_3^2}{4\pi}r\frac{\mathrm{e}^{-3m_\sigma r}}{r}+J_{00}(E)\delta(r)\,.\end{aligned} \tag{41}$$

The exchange term is written as

$$J_{00}(E) = -276\left[1-0.005\frac{E_{\mathrm{Lab}}}{A_{\mathrm{p}}}\right]\ \mathrm{MeV\,fm^3}\,, \tag{42}$$

where E_{Lab} and A_{p} are the incident energy and mass number of the projectile, respectively. The parameters of eleven different NN interaction potentials which consist of HS [35], Z [35], W [35], L1 [35], L2 [35], L3 [35], TS [36],

NL1 [35], NL2 [35], NL3 [37], and NL3* [38] are listed in Table 1. Thus, we can discuss the similarities and differences of various NN interactions investigated in this study.

Table 1. The values of the m_σ (in MeV), m_w (in MeV), m_ρ (in MeV), g_σ, g_w, g_ρ, g_2, and g_3 parameters of different NN interactions including HS, Z, W, L1, L2, L3, TS, NL1, NL2, NL3, and NL3* interactions.

Parameter	m_σ	m_w	m_ρ	g_σ	g_w	g_ρ	g_2	g_3
HS	520	783	770	10.4814	13.8144	8.08488	—	—
Z	551.31	780	763	11.1933	13.8256	10.8883	—	—
W	550	783	—	9.57371	11.6724	—	—	—
L1	550	783	—	10.2999	12.5999	—	—	—
L2	546.940	780	763	11.3972	14.2478	—	—	—
L3	492.260	780	763	10.6920	14.8705	—	—	—
TS	597.6	783	770	11.2060	12.7200	2.78	—	—
NL1	492.250	795.359	763	10.1377	13.2846	9.95145	−12.1724	−36.2646
NL2	504.890	780	763	9.11122	11.4928	10.7732	−2.30404	13.7844
NL3	508.194	782.501	763	10.2170	12.8680	4.474	−10.4310	−28.885
NL3*	502.5742	782.6	763	10.0944	12.8065	4.5748	−10.8093	−30.1486

7. Results and discussion

The theoretical calculations consist of four different stages. We first applied the parameters reported in Ref. [5] as starting values of the optical model parameters for the entrance and exit channels. Then, we performed the parameter search in order to obtain the best fit with the experimental data. In order to reduce ambiguity in the fitting procedure, the geometrical parameters (radius and diffuseness) are usually fixed to average values, and then the potential depths (V_0, W_v, W_d, and $V_{\rm so}$) are adjusted to improve the fit quality. In all the calculations, $r_w = 1.05$ fm, $a_w = 0.18$ fm, $r_{\rm so} = 1.36$ fm, and $a_{\rm so} = 1.18$ fm for the ^{3}He + ^{6}Li channel, $r_v = 1.15$ fm, $a_v = 0.81$ fm, $r_d = 1.34$ fm, $a_d = 0.87$ fm, $r_{\rm so} = 1.15$ fm, and $a_{\rm so} = 0.81$ fm for the $d + ^7$Be channel, and $r_v = 1.15$ fm, $a_v = 0.83$ fm, $r_d = 1.34$ fm, $a_d = 0.90$ fm, $r_{\rm so} = 1.07$ fm, and $a_{\rm so} = 0.66$ fm for the $d + ^6$Li channel. In the folding model calculations, we also fixed the renormalisation factor ($N_{\rm r}$) as one and did not change its default value (≈ 1.0). Thus, we eliminated the effect of the $N_{\rm r}$ value on the cross-section calculations. Finally, we listed the determined values for each approach in tables.

Due to investigating a lot of densities, potentials, or NN interactions, it can be difficult to interpret the harmony between theory and experiment. In this respect, Spatafora *et al.* [39] have presented a quality factor (qf(θ_i))

which is used to check against, in a quantitative manner, the agreement between the theoretical results and the experimental data. The $\mathrm{qf}(\theta_i)$ can be shown by

$$\mathrm{qf}(\theta_i) = \frac{1}{1 + \left|\ln \frac{\sigma_{\mathrm{theo}}(\theta_i)}{\sigma_{\mathrm{exp}}(\theta_i)}\right|}\,, \tag{43}$$

where σ_{exp} and σ_{theo} are the measured and theoretical values of the cross sections at the θ_i scattering angle, respectively. The $\mathrm{qf}(\theta_i)$ can receive values between 0 and 1 according to the worst and best agreements between the results and data, respectively. Then, the quality factor (QF) is calculated for each investigated angular distribution as an arithmetic average of the N_{points} measurements at different angles applying the formula given by

$$\mathrm{QF} = \frac{\sum_i \mathrm{qf}(\theta_i)}{N_{\mathrm{points}}}\,. \tag{44}$$

In this study, the QF values for all analyses of the ^{6}Li(^{3}He,d)^{7}Be transfer reaction are calculated and given in tables.

7.1. Analysis with different density distributions

Here, the transfer cross section of the ^{6}Li(^{3}He,d)^{7}Be reaction at 34 MeV was analyzed for four different density distributions of the ^{3}He nucleus consisting of G1, G2, Ngo, and S. The radial changes of the densities are displayed in Fig. 2. The G1 density is the highest in the center, and the S density is the lowest. However, it was seen that the G1 has the shortest and the S the longest tailing.

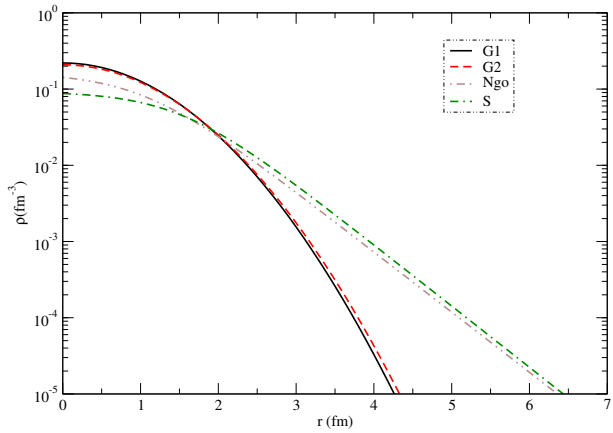

Fig. 2. The changes with the distance of G1, G2, Ngo, and S density distributions in logarithmic scale.

We calculated the transfer cross section of the ^{6}Li(^{3}He,d)^{7}Be reaction at 34 MeV. Then, we performed similar calculations for 33 MeV in order to make a comparative analysis. We compared the results together with the experimental data in Fig. 3 (a)–(b). We also listed the optical potential parameters used in obtaining the results in Table 2. For 34 MeV, we observed that the properties of the results based on the densities were very similar to each other at small angles. On the other hand, there are differences in the results at forward angles. We can see the similar properties of the results of Ngo and S, and G1 and G2. When we compared the theoretical results with the experimental data, we observed that our results are in good agreement with the data, especially at small angles. For 33.3 MeV, the properties of the results were very similar to each other at all angles, and the agreement between the results and the data is very good. Moreover, it was seen from the QF values that the S density is better than other densities in agreement with the data for both 33.4 and 34 MeV energies. Additionally, we can say that these densities can be used as alternative density distributions for the analysis of the ^{6}Li(^{3}He,d)^{7}Be transfer reaction.

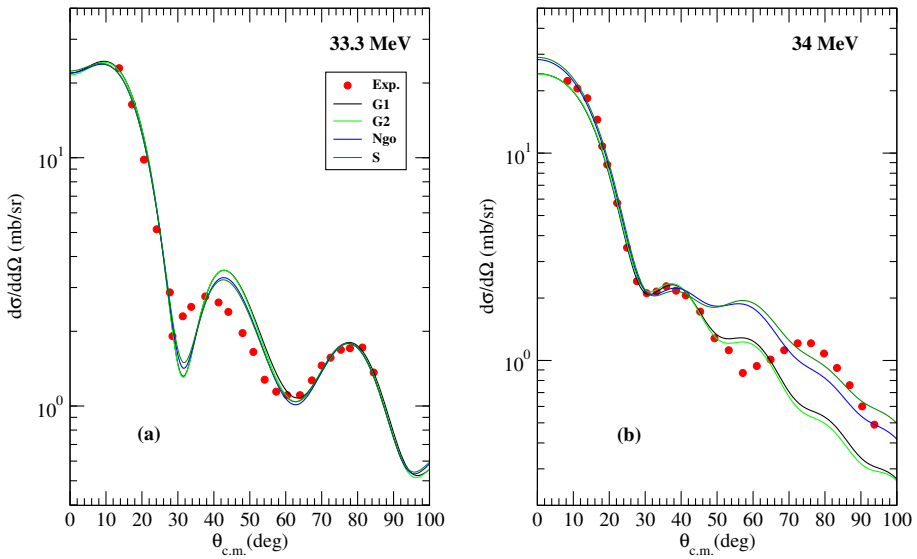

Fig. 3. The cross sections of the ^{6}Li(^{3}He,d)^{7}Be transfer reaction calculated by using G1, G2, Ngo, and S densities in comparison with the experimental data [44] at (a) 33.3 MeV, (b) 34 MeV.

Table 2. The optical model parameters of the entrance channel, exit channel, and core–core potentials used in different density distribution calculations at 34 MeV and quality factors.

Potential [MeV]	G1	G2	Ngo	S
	$^{3}\mathrm{He} + {}^{6}\mathrm{Li}$			
W_v	37.0	41.0	31.0	30.0
V_{so}	6.0	5.80	6.00	5.50
	$d + {}^{7}\mathrm{Be}$			
V_0	50.0	50.0	50.0	51.0
W_d	13.9	13.9	12.9	12.1
V_{so}	3.30	3.90	4.30	5.30
	$d + {}^{6}\mathrm{Li}$			
V_0	84.0	84.0	90.3	86.5
W_d	1.80	1.50	3.00	3.40
V_{so}	6.76	6.76	6.76	6.76
QF-34	0.845	0.837	0.865	0.870
QF-33.3	0.864	0.868	0.876	0.883

7.2. Analysis with temperature-dependent density

The initial state of a transfer reaction is generally assumed as zero temperature [40]. If a nuclear interaction collision between the projectile and target nuclei occurs, an increase in temperature can be carried out [41, 42]. This case can cause a change in density distribution, and the temperature-dependent densities can present differences according to cold nucleus densities [43]. Additionally, it can be said that there is not enough study in the literature in order to interpret the temperature-dependent effect of transfer reactions. Therefore, evaluating little known temperature-dependent density in the literature and reporting alternative approaches for the theoretical analysis of cross sections of transfer reactions can be precious in explaining both existing experimental data and future transfer studies.

In this manner, we examined the effect of temperature-dependent densities of the target nucleus in the entrance channel on the $^{6}\mathrm{Li}(^{3}\mathrm{He},d)^{7}\mathrm{Be}$ transfer cross section. We used the $2pF$ density distribution for temperature-dependent (T = 1, 2, 3, 4, 5, 6, and 7 MeV) and temperature-independent (T = 0 MeV) calculations of the ^{6}Li nucleus. The temperature value is evaluated around 7 MeV as the nucleus can be unstable for much higher

temperatures. We calculated the density distributions based on the temperature, and presented the distance-dependent variations of the densities in Fig. 4. We observed that the density distributions of the ^{6}Li nucleus change with varying temperature. As a result, we can say that the densities in the center decrease with increasing temperature, and the tailing of densities increases with increasing temperature.

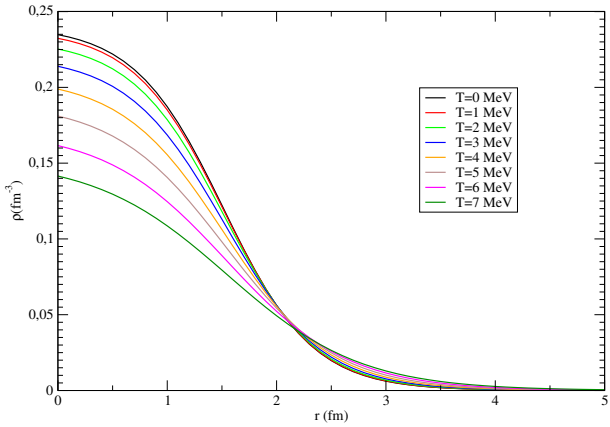

Fig. 4. The changes with the distance of the density distributions of the ^{6}Li nucleus for $T = 0$, 1, 2, 3, 4, 5, 6, and 7 MeV in a linear scale.

Then we calculated the transfer cross sections for the densities depending on the temperature for both 33.4 and 34 MeV energies. We compared the theoretical results and the experimental data in Fig. 5 (a)–(b). We also listed the optical-potential parameters for all the channels in Table 3. We first searched the optical-model parameters to obtain good agreement with the data for $T = 0$ MeV. Then, we applied them, without changing the optical-potential parameters used in the $T = 0$ MeV case, for the temperature-

Table 3. The optical-model parameters of the entrance channel, exit channel, and core–core potentials used in the analysis with temperature-dependent density at 34 MeV.

Channel	V_0 [MeV]	W_v [MeV]	W_d [MeV]	V_{so} [MeV]
^{3}He + ^{6}Li	—	15.0	—	3.0
d + ^{7}Be	53.0	—	12.1	1.3
d + ^{6}Li	71.0	—	2.0	6.76

dependent calculations. Our aim is to see only the temperature-dependent effect without a parameter change. We observed that the results were slightly different from each other. As a result, we can say that the temperature changes the cross section by a certain amount.

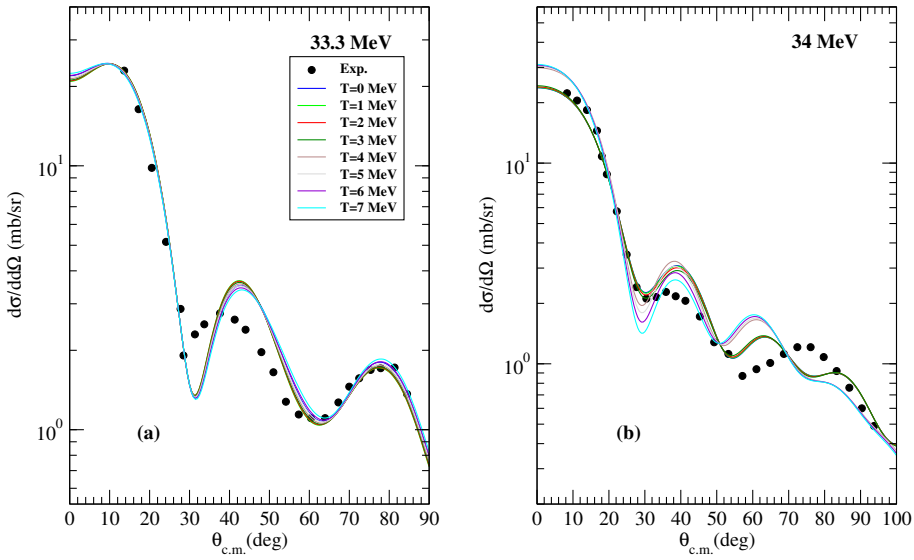

Fig. 5. The cross sections of the ^{6}Li(^{3}He,d)^{7}Be transfer reaction for the densities of the ^{6}Li nucleus for T = 0, 1, 2, 3, 4, 5, 6, and 7 MeV at (a) 33.3 MeV [44], (b) 34 MeV [44].

7.3. Analysis with different nuclear potentials

The achievement of potential parameters for the analysis of transfer reactions is troublesome. In this context, the theoretical analysis is more difficult if the number of free parameters of the investigated potentials increase. In other words, it is very important and useful to find a suitable and alternative potential that describes the analyzed nuclear reaction. As far as we know, there is not enough study in the literature to interpret different proximity-type potentials in the analysis of transfer reactions. For this reason, it would be useful to investigate different nuclear potentials for the analysis of the cross section of the ^{6}Li(^{3}He,d)^{7}Be transfer reaction.

In the present study, we examined the effects of the ^{6}Li(^{3}He,d)^{7}Be transfer reaction of nine different potentials which consist of Prox 77, Prox 88, AW 95, Bass 73, Bass 77, Bass 80, BW 91, CW 76, and Ngo 80 for the entrance channel on the cross section. In this respect, we demonstrated the distance-dependent variations of the potentials in Fig. 6.

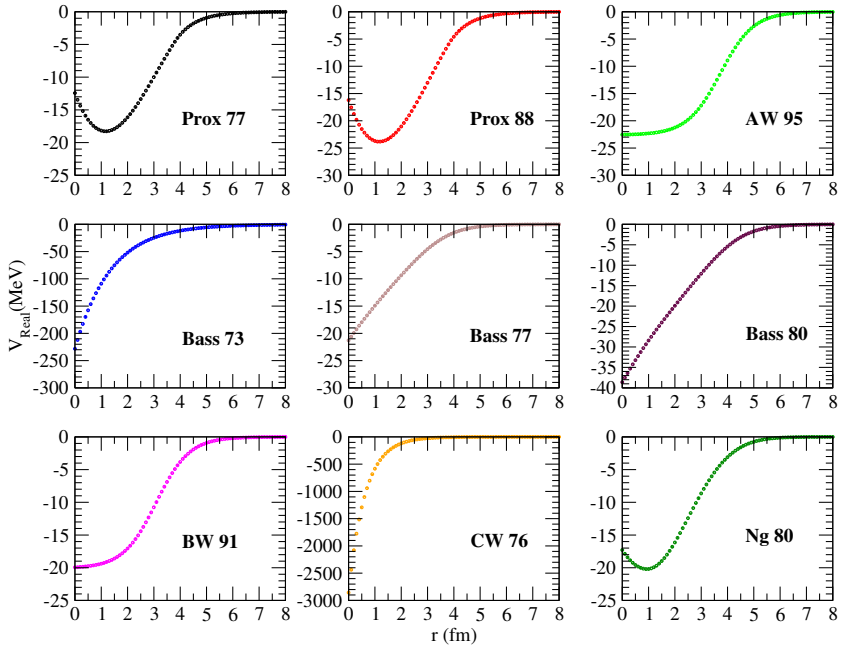

Fig. 6. Distance-dependent changes of Prox 77, Prox 88, AW 95, Bass 73, Bass 77, Bass 80, BW 91, CW 76, and Ngo 80 potentials.

We compared the calculated transfer cross sections with the experimental data in Fig. 7 (a)–(b). We listed the optical potential parameters for all the channels in Table 4. For 34 MeV, the results are generally different from each other. The results of Prox 77, BW 91, and Ngo 80 potentials captured the phase and amplitude of the experimental data very well up to an angle of $\Theta = 70°$. On the other hand, the Bass 77 and CW 76 results are inconsistent with both mid and forward angles of the data, except for small angles. The AW 95 result is in agreement with the experimental data at both small and forward angles, except for some mid-angles of the data. We also observed from the QF values that the AW 95, Bass 73, and Bass 80 potentials are better than the results of the other potentials in agreement with the data. For 33.3 MeV, the results, except for AW 95 and Bass 73, were in good agreement with each other. The AW 95 result, except for $54° < \Theta < 68°$, is in very good agreement with the experimental data at both small and forward angles. Additionally, it was realized from the QF values that the AW 95 potential is better than the results of the other potentials in agreement with the data. It should also be emphasized that the AW 95 potential is a common potential for both energies. Therefore, it can be especially stated that the AW 95 potential together with the other potentials can be used as an alternative potential in analyzing the ^{6}Li(^{3}He,d)^{7}Be transfer reaction.

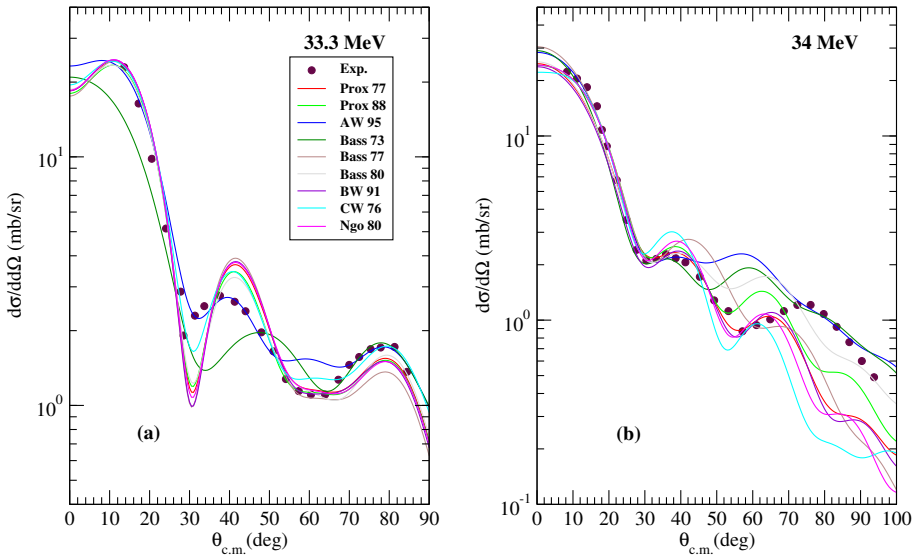

Fig. 7. The cross sections of the ^{6}Li(^{3}He,d)^{7}Be transfer reaction calculated by using Prox 77, Prox 88, AW 95, Bass 73, Bass 77, Bass 80, BW 91, CW 76, and Ngo 80 potentials in comparison with the data [44] at (a) 33.3 MeV, (b) 34 MeV.

Table 4. The optical model parameters of the entrance channel, exit channel, and core–core potentials used in the calculations of different nuclear potentials at 34 MeV and quality factors.

Potential [MeV]	Prox 77	Prox 88	AW 95	Bass 73	Bass 77	Bass 80	BW 91	CW 76	Ngo 80
	^{3}He + ^{6}Li								
W_v	8.00	15.0	24.0	24.0	6.00	10.0	10.0	16.0	16.0
V_{so}	2.20	2.00	6.00	2.00	1.00	2.00	1.00	1.60	1.40
	d + ^{7}Be								
V_0	50.0	50.0	50.0	50.0	50.0	50.0	50.0	50.0	50.0
W_d	15.9	14.5	12.9	12.9	12.9	12.9	15.9	15.9	15.9
V_{so}	9.50	9.50	5.00	8.00	8.00	8.00	8.00	8.00	9.00
	d + ^{6}Li								
V_0	58.0	58.0	90.0	68.0	58.0	58.0	58.0	58.0	58.0
W_d	1.30	1.30	1.10	1.10	1.10	1.10	1.10	1.10	1.10
V_{so}	9.76	9.76	6.76	6.76	6.76	6.76	6.76	6.76	6.76
QF-34	0.828	0.841	0.861	0.868	0.797	0.854	0.814	0.763	0.809
QF-33.3	0.856	0.874	0.903	0.838	0.823	0.876	0.846	0.888	0.844

7.4. Analysis with different NN interactions

Finally, we examined the effects on the cross section of the ^{6}Li(^{3}He,d)^{7}Be transfer reaction of eleven different NN interaction potentials which consist of HS, Z, W, L1, L2, L3, TS, NL1, NL2, NL3, and NL3*. We produced the real potentials of the entrance channel by using these NN interactions. We presented the changes with the distance of all the NN interactions as well as M3Y in Fig. 8. We observed that the shallowest potential belonged to NL2 and the deepest potential belonged to L2 potential.

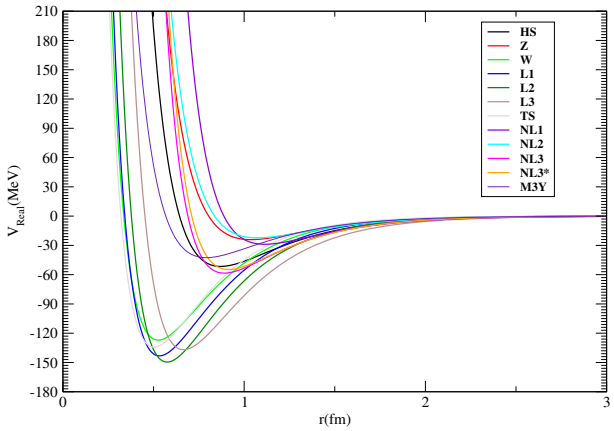

Fig. 8. Distance-dependent changes of the HS, Z, W, L1, L2, L3, TS, NL1, NL2, NL3, and NL3* interactions.

We showed the calculated cross sections together with the experimental data for 33.4 and 34 MeV energies in Fig. 9, and listed the optical potential parameters of all the NN interactions in Table 5. For 34 MeV, we observed that the results of different NN interactions display similarities and differences. We realized that the Z, NL1, and NL2 results are generally far from describing the experimental data. The results with the W, L1, L2, and TS interactions present generally a similar behavior to each other. The result with the HS interaction were generally good in describing experimental data. Additionally, the QF values presented that the result with the HS interaction is better than the results of the other NN interactions. For 33.3 MeV, the results demonstrated similarities and differences with each other. It was found from the QF values that the HS, W, and, especially, TS interactions are better than the results of the other NN interactions. However, we can particularly stress that HS due to becoming a common interaction for both energies can be an alternative NN interaction to the M3Y interaction for the analysis of the ^{6}Li(^{3}He,d)^{7}Be transfer reaction.

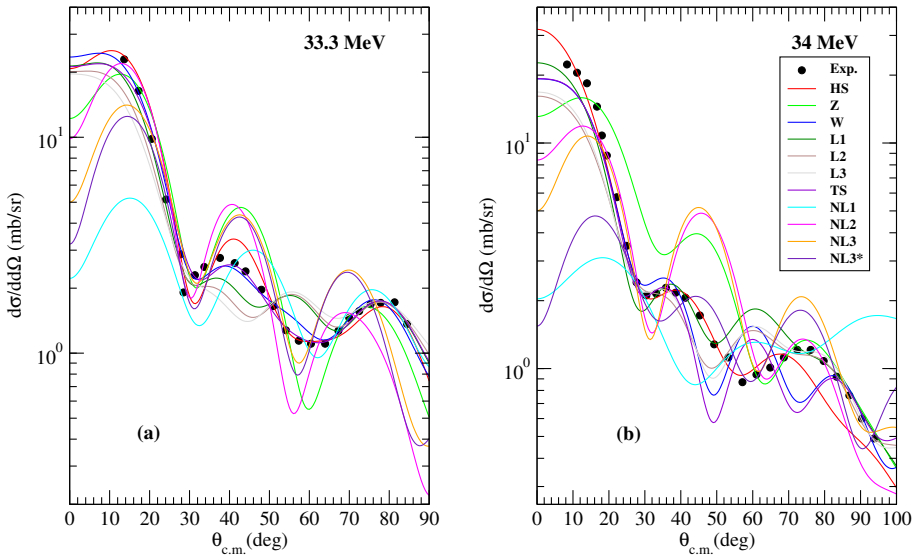

Fig. 9. The cross sections of the ^{6}Li(^{3}He,d)^{7}Be transfer reaction calculated by using the HS, Z, W, L1, L2, L3, TS, NL1, NL2, NL3, and NL3* interactions in comparison with the data [44] at (a) 33.3 MeV, (b) 34 MeV.

Table 5. The optical model parameters of the entrance channel, exit channel, and core–core potentials used in the calculations of different NN interactions at 34 MeV and quality factors.

Potential [MeV]	HS	Z	W	L1	L2	L3	TS	NL1	NL2	NL3	NL3*
	^{3}He + ^{6}Li										
W_v	6.00	8.00	8.00	9.00	9.00	7.00	11.0	7.00	17.0	24.0	11.0
V_{so}	1.30	1.00	2.00	3.30	5.30	4.30	2.00	1.30	2.00	2.00	2.00
	d + ^{7}Be										
V_0	57.0	57.0	57.0	49.0	51.0	51.0	57.0	1.00	41.0	41.0	57.0
W_d	12.9	7.50	11.5	13.5	13.5	13.5	11.5	11.5	11.50	9.50	7.50
V_{so}	6.00	5.00	3.50	2.50	2.50	2.50	3.50	2.50	2.50	1.50	1.50
	d + ^{6}Li										
V_0	90.0	97.0	97.0	87.0	87.0	87.0	97.0	87.0	97.0	97.0	97.0
W_d	1.80	11.0	6.00	1.80	1.80	1.20	5.00	1.20	4.20	4.20	5.00
V_{so}	6.76	6.76	6.76	6.76	6.76	6.76	6.76	6.76	6.76	6.76	6.76
QF-34	0.901	0.762	0.843	0.859	0.847	0.845	0.838	0.673	0.766	0.752	0.763
QF-33.3	0.890	0.798	0.922	0.873	0.840	0.819	0.932	0.788	0.776	0.773	0.759

8. Summary and conclusions

In the present study, we have performed a global investigation of the ^{6}Li(^{3}He,d)^{7}Be transfer reaction at energy of 34 MeV for temperature-dependent and temperature-independent density distributions, different nuclear potentials, and different NN interactions. To make a comparative analysis, we have performed similar calculations for the 33.3 MeV energy value of this reaction. The transfer cross sections have been obtained by using the FRESCO code based on the DWBA method. Also, the double-folding model has been used to calculate the real part of the optical potential.

As a result of these, we have observed that these densities can be used as alternative density distributions for the analysis of the ^{6}Li(^{3}He,d)^{7}Be transfer reaction. Moreover, we have found from the QF values that the S density is in better agreement with the data for both 33.4 and 34 MeV energies than the other densities.

We have examined the effect of temperature-dependent density on the cross section of the ^{6}Li(^{3}He,d)^{7}Be transfer reaction. We have noticed that the temperature somewhat changes both density distribution and cross section.

We have also evaluated nuclear potentials in the theoretical analysis of the transfer reaction. We have proposed that the proximity potentials can be used as alternative potentials in describing the ^{6}Li(^{3}He,d)^{7}Be transfer data. Additionally, we can say that especially the AW 95 potential is in better agreement with the data for each energy than the results of the other potentials.

Finally, we have searched for the NN interactions that can be an alternative to the M3Y interaction. In this manner, we have proposed different alternative NN interactions for the ^{6}Li(^{3}He,d)^{7}Be transfer reaction. Moreover, we have obtained that HS due to becoming a common interaction for both energies can be an alternative NN interaction to the M3Y interaction for the analysis of the ^{6}Li(^{3}He,d)^{7}Be transfer reaction.

In summary, this work presents an important step towards understanding the effect of different densities, temperatures, nuclear potentials, and NN interactions on the cross section of the ^{6}Li(^{3}He,d)^{7}Be transfer reaction. The results demonstrate that our understanding of the structure of the ^{6}Li(^{3}He,d)^{7}Be transfer reaction requires further attention. In this context, we would like to point out that Burtebayev *et al.* [5] reported the necessity of CRC corrections in their calculations. Additionally, further investigations and applications by taking into account the ANCs model for the ^{3}He + ^{4}He or p + ^{6}Li channels would provide a stronger physical case. In the same way, it could be useful to extend the calculations to ^{3}He + ^{6}Li elastic scattering or different ^{7}Be excited states. We could not take these effects

into account because we performed different and multi-alternative calculations in our study. Therefore, it is not possible at present to provide such a theoretical analysis and further work in order not to go beyond the scope of this study and not to increase the calculations even more. However, we can state that all of these can be evaluated as subjects that should be examined separately in future studies. Based on the results of this study, we consider that it would be interesting and helpful to apply these interactions to other transfer reactions.

The authors are very grateful to the Scientific and Technological Research Council of Türkiye (TUBITAK) for the financial support (Project Number: 122F275). The authors would also like to thank the anonymous referee for the useful comments and suggestions for improving the manuscript.

REFERENCES

[1] W.R. Phillips, «Heavy-ion transfer reactions», *Rep. Prog. Phys.* **40**, 345 (1977).

[2] D. Bardayan, «Transfer reactions in nuclear astrophysics», *J. Phys. G: Nucl. Part. Phys.* **43**, 043001 (2016).

[3] H. Lüdecke, T. Wan-Tjin, H. Werner, J. Zimmerer, «The reactions ^{6}Li^{3}He, ^{3}He$_0$)^{6}Li, ^{6}Li$(d, d_0)^{6}$Li, ^{7}Li$(d, d_0)^{7}$Li and ^{6}Li$(^{3}$He, $d_{0,1})^{7}$Be», *Nucl. Phys. A* **109**, 676 (1968).

[4] A.K. Basak *et al.*, «Polarization effects in ^{3}He induced transfer reactions on lithium isotopes», *Nucl. Phys. A* **368**, 93 (1981).

[5] N. Burtebayev *et al.*, «Effects of t- and α-transfer on the spectroscopic information from the ^{6}Li(^{3}He, $d)^{7}$Be reaction», *Nucl. Phys. A* **909**, 20 (2013).

[6] N. Burtebayev *et al.*, «Effect of the Transfer Reactions for ^{16}O+^{10}B Elastic Scattering», *Acta Phys. Pol. B* **50**, 1423 (2019).

[7] I.J. Thompson, «Coupled reaction channels calculations in nuclear physics», *Comput. Phys. Rep.* **7**, 167 (1988).

[8] J. Cook, «DFPOT — A program for the calculation of double folded potentials», *Comput. Phys. Commun.* **25**, 125 (1982).

[9] M. Aygun, «A Microscopic Analysis of Elastic Scattering of ^{8}Li Nucleus on Different Target Nuclei», *Acta Phys. Pol. B* **45**, 1875 (2014).

[10] M. Aygun, «A comparative analysis of the density distributions and the structure models of ^{9}Li», *Pramana* **88**, 53 (2017).

[11] M. Aygun, «Double-folding analysis of the ^{6}Li + ^{58}Ni reaction using the *ab initio* density distribution», *Eur. Phys. J. A* **48**, 145 (2012).

[12] M. Aygun, Y. Kucuk, I. Boztosun, A.A. Ibraheem, «Microscopic few-body and Gaussian-shaped density distributions for the analysis of the ^{6}He exotic nucleus with different target nuclei», *Nucl. Phys. A* **848**, 245 (2010).

[13] M. Aygun, Z. Aygun, «A theoretical study on different cluster configurations of the ^{9}Be nucleus by using a simple cluster model», *Nucl. Sci. Tech.* **28**, 86 (2017).

[14] M. Aygun, «Reanalysis of Elastic Scattering of ^{6}Li + ^{209}Bi Reaction Using a New Density Distribution of ^{6}Li Nucleus», *Commun. Theor. Phys.* **60**, 69 (2013).

[15] F.S. Chwieroth, Y.C. Tang, D.R. Thompson, «Microscopic coupled-channel study of the five-nucleon system with the resonating-group method», *Phys. Rev. C* **9**, 56 (1974).

[16] Sh. Hamada, «Coupled Reaction Channels and Cluster Folding Analysis for ^{3}He + ^{20}Ne Elastic and Inelastic Scattering», *Phys. Part. Nucl. Lett.* **16**, 602 (2019).

[17] C. Ngô *et al.*, «Properties of heavy ion interaction potentials calculated in the energy density formalism», *Nucl. Phys. A* **252**, 237 (1975).

[18] H. Ngô, C. Ngô, «Calculation of the real part of the interaction potential between two heavy ions in the sudden approximation», *Nucl. Phys. A* **348**, 140 (1980).

[19] H. Schechter, L.F. Canto, «Proximity formulae for folding potentials», *Nucl. Phys. A* **315**, 470 (1979).

[20] R.K. Gupta, D. Singh, W. Greiner, «Semiclassical and microscopic calculations of the spin-orbit density part of the Skyrme nucleus–nucleus interaction potential with temperature effects included», *Phys. Rev. C* **75**, 024603 (2007).

[21] S. Shlomo, J.B. Natowitz, «Temperature and mass dependence of level density parameter», *Phys. Rev. C* **44**, 2878 (1991).

[22] J. Błocki, J. Randrup, W.J. Świątecki, C.F. Tsang, «Proximity forces», *Ann. Phys. (NY)* **105**, 427 (1977).

[23] I. Dutt, R.K. Puri, «Comparison of different proximity potentials for asymmetric colliding nuclei», *Phys. Rev. C* **81**, 064609 (2010).

[24] W.D. Myers, W.J. Swiatecki, «Nuclear masses and deformations», *Nucl. Phys.* **81**, 1 (1966).

[25] W. Reisdorf, «Heavy-ion reactions close to the Coulomb barrier», *J. Phys. G: Nucl. Part. Phys.* **20**, 1297 (1994).

[26] L. Zhang *et al.*, «Moments of the three-parameter Fermi distribution», *Mod. Phys. Lett. A* **32**, 1750195 (2017).

[27] A. Winther, «Dissipation, polarization and fluctuation in grazing heavy-ion collisions and the boundary to the chaotic regime», *Nucl. Phys. A* **594**, 203 (1995).

[28] R. Bass, «Threshold and angular momentum limit in the complete fusion of heavy ions», *Phys. Lett. B* **47**, 139 (1973).

[29] R. Bass, «Fusion of heavy nuclei in a classical model», *Nucl. Phys. A* **231**, 45 (1974).

[30] R. Bass, «Nucleus–Nucleus Potential Deduced from Experimental Fusion Cross Sections», *Phys. Rev. Lett.* **39**, 265 (1977).

[31] P.R. Christensen, A. Winther, «The evidence of the ion–ion potentials from heavy ion elastic scattering», *Phys. Lett. B* **65**, 19 (1976).

[32] R. Brockmann, «Relativistic Hartree–Fock description of nuclei», *Phys. Rev. C* **18**, 1510 (1978).

[33] L.D. Miller, A.E.S. Green, «Relativistic Self-Consistent Meson Field Theory of Spherical Nuclei», *Phys. Rev. C* **5**, 241 (1972).

[34] R. Brockmann, W. Weise, «Spin-orbit coupling in a relativistic Hartree model for finite nuclei», *Phys. Rev. C* **16**, 1282 (1977).

[35] P.G. Reinhard, «The relativistic mean-field description of nuclei and nuclear dynamics», *Rep. Prog. Phys.* **52**, 439 (1989).

[36] H. Toki *et al.*, «Properties of nuclei far from the stability line in the relativistic Hartree theory», *Nucl. Phys. A* **524**, 633 (1991).

[37] G.A. Lalazissis, J. König, P. Ring, «New parametrization for the Lagrangian density of relativistic mean field theory», *Phys. Rev. C* **55**, 540 (1997).

[38] G.A. Lalazissis *et al.*, «The effective force NL3 revisited», *Phys. Lett. B* **671**, 36 (2009).

[39] A. Spatafora *et al.*, «Multichannel experimental and theoretical approach to the ^{12}C(^{18}O,^{18}F)^{12}B single-charge-exchange reaction at 275 MeV: Initial-state interaction and single-particle properties of nuclear wave functions», *Phys. Rev. C* **107**, 024605 (2023).

[40] M. Aygun, Z. Aygun, «A comprehensive analysis of ^{9}Li + ^{70}Zn fusion cross section by using proximity potentials, temperature dependent density distributions and nuclear potentials», *Rev. Mex. Fis.* **65**, 573 (2019).

[41] L. Guo-Qiang, X. Gong-Ou, «Optical potential and the fusion barrier of two hot nuclei», *Phys. Rev. C* **41**, 169 (1990).

[42] M. Rashdan, A. Faessler, M. Ismail, N. Ohtsuka, «The temperature dependence of the Hi optical potential», *Nucl. Phys. A* **468**, 168 (1987).

[43] R.K. Puri *et al.*, «Temperature-dependent mean field and its effect on heavy-ion reactions», *Nucl. Phys. A* **575**, 733 (1994).

[44] `https://www-nds.iaea.org/exfor/`